Form Drag on Ocean Flows

Parker MacCready, Geno Pawlak[+], Kate Edwards, and Ryan McCabe

University of Washington, Seattle, WA, USA
[+]University of Hawaii, Honolulu, HI

Abstract. Form drag is a central process linking rough topography to ocean mixing processes. The history of the measurement of form drag in the ocean and atmosphere is reviewed. The basic equations governing form drag and its role in energy conversion are derived for a Boussinesq fluid, focusing on the case of tidal flow. Observational and numerical results are shown for stratified, tidal flow near a headland in Puget Sound, Washington. There the net form drag far exceeds the frictional drag. Speculative comments are made concerning when and where form drag is likely to be important.

Introduction and a Brief History

We all understand form drag (sometimes called "pressure drag"). It is simply the spatial integral of bottom pressure times bottom slope (*Baines,* 1995, p.13; *Kundu and Cohen*, 2002, p. 338; *Gill*, 1982, p. 145). It is also often quantified higher in the water column as the vertical Reynolds stress due to waves, as in Gill. Similarly, the rate of doing work by the form drag is intuitively obvious. It is just the form drag times the speed of the interior flow. However, there are times when these simple definitions can be troublesome. For example, in a container of motionless fluid shaped like a pint of beer, the boundary pressure times the boundary slope (in the vertical direction) has a non-zero integral. Yet we intuitively know that there is no real form drag in this case, so is there a problem with our definition? Similarly, when the flow is tidal, or it is difficult to define an undisturbed interior flow, what is the rate of doing work by the form drag? When is it appropriate to calculate form drag on an isolated feature, when the feature is not an isolated Gaussian bump, but is instead part of a deeply-incised continental slope? Further, how is it that form drag can be part of an energy equation when the boundary is stationary, and hence can do no work? Questions such as these are motivation for including here a rigorous derivation of the form drag, and its role in energy conversion.

First studied in aeronautics, form drag is ubiquitous in geophysical flows such as airflow over mountains. *Smith* (1978) measured the form drag on a small mountain using a number of microbarographs at ground stations. He discusses in detail the problems facing this seemingly direct approach. The main source of error is that one does not know the absolute height of the instrument to great enough accuracy (1 m in his case!). To get around this he reasoned that if you could just find a time with very little wind in the record, then you could use that to determine absolute pressures for each record. Atmospheric scientists have refined this approach, and have also used aircraft measurements to try to determine vertical momentum fluxes in sections above mountains. Many of these are reviewed in *Davies and Phillips* (1985). *Hafner and Smith* (1985) used a 2-D array of microbarographs in the Alps to get form drag vectors, instead of just looking at it as a process acting normal to a ridge crest. The physical processes which give rise to form drag can be either the generation of internal waves, or flow separation. The drag exerted can be substantial, ranging from about equal to the frictional drag up to 10 times that value for the Southern Alps of New Zealand. Since the flows which generate form drag are typically of much smaller scale than those resolved by atmospheric numerical models, there has been considerable work on the parameterizing of form drag, as exemplified by *Lott and Miller* (1997). They find significant improvements in predicted flow result for flow over mountains. A nice review of both the physics and the forecasting implications is given by *Schär* (2002).

In contrast to atmospheric studies, estimates of form drag generated by oceanic obstacles are extremely rare, because it is difficult to make highly spatially resolved bottom pressure measurements

across an obstacle. Modern pressure sensors do have the required accuracy to measure the pressure signals associated with coastal form drag processes. But just knowing the bottom pressure does not tell you all you might like to know about the flow, such as why there is form drag in a given place. The scale of topographic obstacles that cause the greatest form drag is not well known, however it is likely to lie somewhere between 20 m (too large to be shielded by the bottom boundary layer), and 10 km (at which point geostrophic flow becomes more important). One of the few oceanic measurements of form drag was made by *Moum and Nash* (2000) and *Nash and Moum* (2001) at Stonewall Bank off the Oregon coast. They found that on this 5-km-long obstacle, form drag exceeded skin friction by a factor of 2-3. The form drag estimate was based on vertically integrated density profiles from the free-falling Chameleon profiler, as it will be in results presented below.

Given the observational difficulties, numerical estimates have provided useful insights into the mechanics of form drag. The increase of the form drag with the height of an isolated ridge on a slope has been simulated by *MacCready and Pawlak* (2001). The same model will be used here to simulate the flow at the Three Tree Point headland in Puget sound, WA. *Thorpe* (1992) found that frictional and form drag were about equally important to drag in a numerical simulation of flow over the corrugated continental slope near Porcupine Bank off England. Numerical models of barotropic tidal flow in Puget Sound (*Lavelle et al*., 1988) and the Strait of Juan de Fuca (*Foreman et al*., 1995) have found that they need a quadratic drag coefficient of $\sim 1-2\times10^{-2}$ in order to match observed patterns of tidal height and phase. This is 5-10 times the usual value.

The great importance of form drag to oceanic flows has recently been highlighted by the observation of enhanced mixing high over the Mid-Atlantic Ridge, presumably driven by the conversion of barotropic tidal flow across the ridge into internal waves (*Ledwell et al.*, 2000; *Jayne and St. Laurent*, 2001). In coastal regions, where the majority of tidal energy is dissipated, the conversion of barotropic tidal currents into eddies, waves, and eventually turbulence, is of intrinsic importance to numerical modelers and ecosystems alike. Form drag can be seen as an intermediary in this conversion.

Basic Momentum Theory

Begin with the Boussinesq equations for momentum, volume, and density:

$$\mathbf{u}_t + \mathbf{u}\cdot\nabla\mathbf{u} + f\hat{\mathbf{k}}\times\mathbf{u} = \frac{-\nabla p'}{\rho_o} - \hat{\mathbf{k}}\frac{g\rho'}{\rho_o} + \nu\nabla^2\mathbf{u} \qquad (1)$$

$$\nabla\cdot\mathbf{u} = 0 \qquad (2)$$

$$\rho'_t + \nabla\cdot\left(\rho'\mathbf{u}\right) + w\bar{\rho}_z = \kappa\nabla^2\left(\bar{\rho}+\rho'\right) \qquad (3)$$

where $\mathbf{u} = (u,v,w)$ is the velocity vector, subscripts *t*, *x*, *y*, *z* denote partial differentiation, f is the Coriolis frequency, $\hat{\mathbf{k}}$ is the vertical unit vector, and ν and κ are the molecular viscosity and diffusivity. The density and pressure have been divided into parts as $\rho = \rho_o + \bar{\rho}(z) + \rho'(\mathbf{x},t)$ and $p = p_o(z) + p'(\mathbf{x},t)$, where $\partial p_o/\partial z = -g(\rho_o + \bar{\rho})$. Note that (1) is a vector equation, and the term $\nabla\mathbf{u} \equiv (\nabla u, \nabla v, \nabla w)$. The form drag arises out of a volume integral of (1). The volume of integration, V, will be bounded by area A consisting of (i) the ocean surface at $z=\eta$, (ii) the ocean floor at $z=\zeta(A_{BOT})$, and (iii) some vertical sides which are arbitrary cuts through the water (A_{SIDES}), as sketched in Fig. 1. The volume integral of (1) is

$$\int_V \mathbf{u}_t \; dV + \int_A \mathbf{u}u_n \; dA + f\int_V \hat{\mathbf{k}}\times\mathbf{u} \; dV$$
$$= -\int_A \frac{p'}{\rho_o}\hat{\mathbf{n}} \; dA - \int_V \hat{\mathbf{k}}\frac{g\rho'}{\rho_o} \; dV + \int_A (\nu\nabla\mathbf{u})\cdot\hat{\mathbf{n}} \; dA \qquad (4)$$

In deriving (4) we have made liberal use of Gauss' Divergence Theorems: $\int_V \nabla\cdot\mathbf{C}\,dV = \int_A \mathbf{C}\cdot\hat{\mathbf{n}}\,dA$ and $\int_V \nabla\psi\,dV = \int_A \psi\,\hat{\mathbf{n}}\,dA$, where $\mathbf{C}$ and ψ are arbitrary vector and scalar fields. Note that (4) is still a vector equation. The outward unit normal to A is $\hat{\mathbf{n}}$, and the normal velocity is $u_n \equiv \mathbf{u}\cdot\hat{\mathbf{n}}$. We have used incompressibility (2) in places to rewrite terms so that the Divergence Theorems can be used with them, for instance: $\mathbf{u}\cdot\nabla u = \nabla\cdot(\mathbf{u}u) + u(\nabla\cdot\mathbf{u}) = \nabla\cdot(\mathbf{u}u)$. Now, consider just the *x*-component of (4), by taking $\hat{\mathbf{i}}\cdot(4)$:

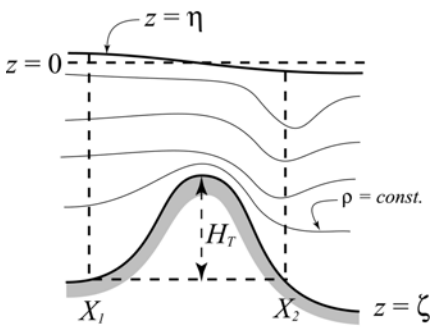

Figure 1. Sketch of 2-D flow over a ridge.

$$\int_V u_t\,dV + \int_A u u_n\,dA - f\int_V v\;\;dV = -\int_A \frac{p'}{\rho_o}\hat{\mathbf{i}}\cdot\hat{\mathbf{n}}\;\;dA + \int_A \nu\frac{\partial u}{\partial n}\;\;dA \qquad (5)$$

To find the form drag, consider just the pressure term in (5), on the bottom area A_{BOT}, which has projected horizontal area A_o. On the surface A_{BOT}, the outward normal unit vector is given by

$$\hat{\mathbf{n}} = \frac{\left(\zeta_x, \zeta_y, -1\right)}{\left(\zeta_x^2 + \zeta_y^2 + 1\right)^{1/2}}, \qquad (6)$$

and $dA_{BOT} = dA_o\left(\zeta_x^2 + \zeta_y^2 + 1\right)^{1/2}$. Hence we find

$$-\int_{A_{BOT}} \frac{p'}{\rho_o}\hat{\mathbf{i}}\cdot\hat{\mathbf{n}}\,dA = -\int_{A_o} \frac{p_B'}{\rho_o}\zeta_x\,dA, \qquad (7)$$

where P_B' is the pressure anomaly on the bottom. Finally, assuming $\rho' = 0$ on $z = \eta$, and $u_n = 0$ on A_{BOT}, we may rewrite the *x*-component of the volume integral of the momentum equations as

$$\int_V u_t\;\;dV + \int_{A_{SIDES}} u u_n\;\;dA - f\int_V v\;\;dV = -\int_{A_{SIDES}} \frac{p'}{\rho_o}\hat{\mathbf{i}}\cdot\hat{\mathbf{n}}\;\;dA - \int_{A_o} \frac{p_B'}{\rho_o}\zeta_x\;\;dA + \int_{A_{BOT}} \nu\frac{\partial u}{\partial n}\;\;dA \qquad (8)$$

Note that the last term may be approximated as $\int_{A_{BOT}} \nu\frac{\partial u}{\partial n}dA \cong -\int_{A_o} \nu u_z\,dA$ when $\zeta_x, \zeta_y << 1$, and $u_x, u_y << u_z$. Equation (8) is the fundamental theoretical expression of the form drag (the term containing p_B'). The form drag is just one of several terms which may affect the net acceleration.

Simple Barotropic Examples

The form drag, and a few of its difficulties, are most easily understood for 2-D, non-rotating, linear, inviscid flow, for which (8) simplifies to

$$\int_{A_H} u_t\,dA = -\left(gh\eta\right)\Big|_{X_1}^{X_2} - \int_{X_1}^{X_2} g\eta\zeta_x\,dx \qquad (9)$$

net acceleration = net forcing - form drag

We have assumed the pressure anomaly is hydrostatic, given by $p'/\rho_o = g\eta$. The area of the 2-D section is A_H and has length L in the *x*-direction, from X_1 to X_2 (Fig. 2).

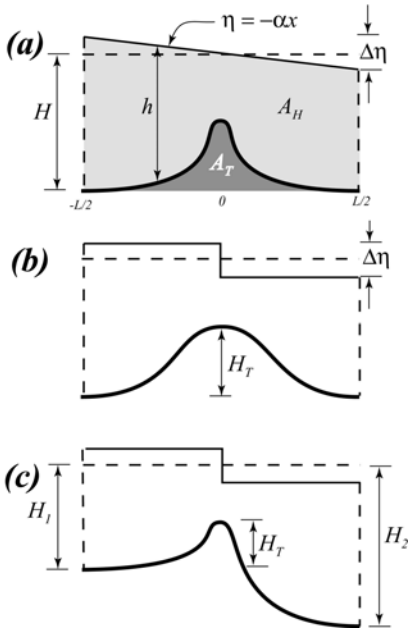

Figure 2. Sketches of 3 different scenarios for 2-D barotropic flow over a ridge.

Consider first a simple case (Fig. 2a) where the surface height has a constant *x*-gradient, $-\alpha$. In this case (9) gives the result:

Case (a): $$\int_{A_H} u_t\,dA = g\alpha HL - g\alpha A_T \qquad (10)$$

where the first term on the RHS is the "net forcing" from (9), and the second term on the RHS is the form drag. Note that the RHS of (10) may also be written as $g\alpha A_H$, which is obvious by inspection. Immediately one becomes suspicious. The "form drag" term

on (10) looks like it is not really a real drag at all, and instead just accounts from the lack of net acceleration because we don't have water to accelerate in the area under the topography. Other aspects of Case (a) in Fig. 2 are also suspect. Usually we associate form drag with physical features like a hydraulic jump, a trapped internal lee wave, or flow separation. Also in Case (a) there is no sense of where the form drag might act in the fluid - where is the fluid that is being slowed down? This unpleasant example is analogous to the vertical "form drag" one might calculate for the hydrostatic, motionless pressure field in a pint of beer (a truncated cone). The sloping sidewalls do help support the beer, but does the *z*-component of the force on them really constitute a form drag? Likewise, Case (a) could be seen as the situation arising in tidal flow at high slack water in a long inlet; the velocity is zero everywhere and is getting ready to take off to the right, yet there is an apparent form drag. One way to reconcile this would be to appeal to energy: if the form drag does no work (as would be the case with no flow) then it is not a "real" form drag. This is discussed further in following sections The reason for belaboring the point above is that we often do want to calculate the form drag of features in tidal flows, and thus we have to decide what to make of this unreal form drag. Also, *Hafner and Smith* (1985) made the explicit assumption that their mountains were embedded in a pressure field with constant gradient, as in our Case (a).

Turning to a more clear-cut example, now assume (Fig. 2b) that the surface height field is flat except for a localized jump of $\Delta\eta$ right at the ridge. In this case (9) gives

Case (b): $$\int_{A_H} u_t \, dA = gH\Delta\eta - gH_T\Delta\eta \qquad (11)$$

and the form drag just depends on the height of the bump and the pressure drop across it. Real flows are often like a mixture of Case (a) and Case (b), because flow driven by a large-scale pressure gradient will have a local response. Again we will appeal to energy arguments to get the real form drag.

A final wrinkle to consider has to do with flow past a ridge which is deeper on one side than the other (Fig. 2c) such as the Mendocino Escarpment. It is often assumed (*Nash and Moum*, 2001, Eq. 8) that the integration of form drag should begin and end at topography of the same depth, as in Fig. 1. But this precludes our being able to address a feature like a back-facing step, which can be anticipated to have form drag. Evaluating (9) for Case (c), we find

$$\int_{A_H} u_t \, dA = g\frac{H_1 + H_2}{2}\Delta\eta - gH_T\Delta\eta - g\left(H_2 - H_1\right)\frac{\Delta\eta}{2} \qquad (12)$$

Here we see that the net forcing term has been sensibly modified to have the mean depth at the edges. Also, there is an extra part to the form drag (the last term on the RHS of 12) which is an additional form drag due to the deep right flank of the ridge. Thus the two last terms in (12) are the correct form drag, so why don't we routinely calculate the form drag over the full ridge? The reason is that it is not always so easy, observationally, to split the density and pressure fields up into the background and anomaly parts. For instance, if we used a slightly different definition for the depth of $z = 0$ in Case (c), it would change the last term in (12), but it would not change the form drag term in (11). By beginning and ending the integration at the same depth, any constant added to the bottom pressure does not change the form drag.

A Baroclinic Example

While the examples above pertained to barotropic hydraulic or tidal flow, form drag also is an important process in baroclinic systems. The simplest is 2-D stratified flow over a corrugated boundary. The solution is obtained (*Gill*, 1982, p. 145) by matching the linear wave solution to the vertical velocity forced at the boundary, and then calculating the form drag as the vertical Reynolds stress, τ_W, at some level above the boundary:

$$\tau_W = -\rho_o \overline{u'w'}^x = \frac{1}{2}\rho_o \delta^2 N^2 F^2 \left(\frac{1}{F^2} - 1\right)^{1/2} \qquad (13)$$

where overbar-*x* denotes averaging over one wavelength, k is the wavenumber of the cosine-corrugated topography, which has amplitude δ. The subscript W is for wave. The flow is characterized by the Froude number $F = Uk/N$ where U is free-stream velocity $(u = U + u')$, and the buoyancy frequency is $N = \left(-g\bar{\rho}_z/\rho_o\right)^{1/2}$. Expression (13) may also be obtained from the bottom pressure times the bottom slope, as in (8). The form drag (13) increases approximately line

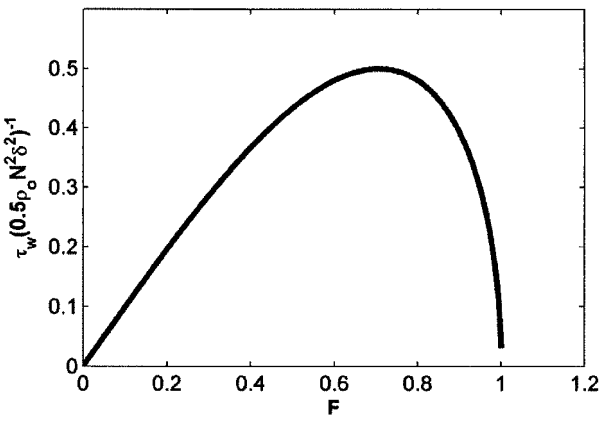

Figure 3. Normalized form stress due to internal wave generation by stratified flow over a corrugated boundary, plotted versus the Froude number, *F*. The maximum stress occurs at F=-$2^{-1/2}$.

arly with F, has a maximum at $F = 2^{-1/2}$, and then drops off steeply to zero as F approaches 1 (Fig. 3). At the high-*F* cutoff the wavecrests become vertical, and the solution becomes evanescent and is thus incapable of sending wave energy away from the ground. The work done by the form drag is given by $U\tau$, and the momentum extracted from the flow only shows up where the wave energy is dissipated, possibly quite remote from the boundary. One may easily show that the maximum rate of doing work, versus k, also occurs at $F = 2^{-1/2}$. This then gives a topographic length scale, the wavelength $\lambda_{\max}$, which, all other things being equal, will extract the most energy from the flow:

$$\lambda_{\max} = \frac{2^{3/2}\pi U}{N} \qquad (14)$$

Assuming a typical coastal stratification $N = 10^{-2}$ s^{-1}, and a range of velocities $U = 0.1-1$ m s^{-1}, we find $\lambda_{\max}$ varies from about 100 m to 1 km (the scales would be about 10 times greater in the deep ocean). These are very small scales, and are not typically resolved by coastal numerical models. However, the true test of the importance of the form drag is whether or not it is greater than the frictional drag of the usual bottom boundary layer. This stress is given by, $\tau_{BBL} = \rho_o C_D U^2$, where C_D is a drag coefficient, typically about 2.5×10^{-3}. Then, assuming that the topography has the maximum drag wavelength (14), the ratio of the two drag terms will be

$$\frac{\tau_{W\max}}{\tau_{BBL}} = \frac{\delta^2 k^2}{2C_D} = \frac{S^2}{2C_D} \qquad (15)$$

where S is the maximum slope angle of the corrugations. This predicts that the form drag will be important when $S \geq 1/10$. The peak of maximum form drag is not very sharp (Fig. 3), so we may expect that (15) will be a reasonable guide even as F varies substantially around the maximum stress.

Form Drag on Quasigeostrophic Flows

Given the small spatial scales implied by (14), we expect that quasigeostrophic flow will have little form drag. Indeed, the introduction of f to the internal wave problem above creates a low-speed cutoff to τ_W (the same is true if the corrugations lie on a slope: *Thorpe* 1992, 1996; *MacCready and Pawlak,* 2001). However, form drag at very large scales has been suggested (*Munk and Palmen*, 1951) as the primary drag on the Antarctic Circumpolar Current (ACC). Further, *Killworth and Nanneh* (1994) proposed that the vertical divergence of form drag on isopycnal layers could be the primary balance for the Coriolis force attendant on the meridional circulation of the ACC. But *Marshall et al*. (1993) pointed out that, by orienting the path of integration in a layer along the time-averaged geostrophic flow (and hence along a path $p' \cong$ const.) that the time-averaged form drag must also vanish (see also *MacCready and Rhines*, 2001). Hence it must only be the form drag on transient eddies which contributes to the actual form drag between layers. This points toward a problem for topographic form drag due to flows which are nearly geostrophic: we can in general find a curved path of integration over the topography upon which $p_B' =$ const., and upon this path the form drag will vanish (assuming we integrate to the same bottom depth at each end). This suggests that the calculations of mountain drag (reviewed for example in *Gill*, 1982) may overstate the importance of form drag at large scales. In contrast, for smaller scale flows which are less affected by rotation (larger Rossby number) no such path exists. In general, the most

"natural" path for a line integral of form drag is probably a time-mean streampath, which may be difficult to achieve except in numerical simulations. But an even better approach in that case is to use the full volume integral (8).

Energy

The conservation equation for energy per unit volume may be written as

$$E_t + \nabla \cdot E\mathbf{u} = \rho_o \mathbf{u} \cdot \Phi - \nabla \cdot \left(p'\mathbf{u} \right) - N, \quad (16)$$

where $E \equiv \left[(1/2)\rho_o \mathbf{u} \cdot \mathbf{u} - (1/2)\left(g\rho'^2 / \overline{\rho}_z \right) \right]$, and N is the net dissipation of kinetic and potential energies due to viscosity and diffusivity. We have included a non-standard term, $\rho_o \mathbf{u}\Phi$ on the RHS of (13). There we have assumed the existence of an extra body force $\Phi = \left(\varphi^x, \varphi^y, \varphi^z \right)$ (a force per unit mass) added to the RHS of the momentum equations (1), which may be a function of time. So the new momentum equation is

$$\mathbf{u}_t + \mathbf{u} \cdot \nabla \mathbf{u} + f\hat{\mathbf{k}} \times \mathbf{u} = \Phi - \frac{\nabla p'}{\rho_o} - \hat{\mathbf{k}} \frac{g\rho'}{\rho_o} + \nu \nabla^2 \mathbf{u} \quad (17)$$

Why do this? The reason is that this is a practical means of forcing a tidal flow in a small (re-entrant) segment of a channel in a numerical simulation (as we do in the final section of this paper). It takes the place of a large-scale gradient of surface height, as in Case (a) of Fig. 2. The volume integral of (16) is

$$\frac{\partial}{\partial t}\left[\int_V E \; dV + \int_{A_o} (1/2)\rho_o g\eta^2 dA \right] + \int_{A_{SIDES}} \mathbf{u} \cdot \hat{\mathbf{n}} \; E \; dA = \rho_o \int_V \mathbf{u} \cdot \Phi \; dV - \int_{A_{SIDES}} \mathbf{u} \cdot \hat{\mathbf{n}} \; p' \; dA - \int_V N \; dV. \quad (18)$$

Now, the interesting thing about (18) is that there is no form drag! It would have appeared as a pressure term on the RHS, but on the bottom $\mathbf{u} \cdot \hat{\mathbf{n}} = 0$, so the term vanishes. Physically, there is no velocity through the boundary for the pressure to work on. Textbooks (e.g., *Gill*, 1982, p. 311) give a neat solution to this problem, which is to transform the system to a frame of reference moving with the free stream flow, U. This is a Galilean transformation if the free stream is steady (and easily defined) and so the basic physics are unaltered. The primary change is that the form drag now enters as a term on the RHS of the energy equation, given by $U\int_{A_o} p_B'\zeta_x \, dA$. This is generally a source of energy because U and $\int_{A_o} p_B'\zeta_x \, dA$ are likely to have the same sign. A nice thing about this frame of reference is that most flow disturbances due to the topography will be source terms in the energy budget, because we are looking at the perturbation energy away from the mean flow U. Of course for a steady mean flow one does not need to resort to the fictitious body force in (17).

What do we do if U is unsteady, or difficult to define (e.g., in a constricted strait or estuarine channel)? Assume that the flow is fundamentally tidal, and we force with

$$\left(\frac{\partial U_T}{\partial t}, 0, 0 \right) = \left(\varphi^x, \varphi^y, \varphi^z \right) \quad (19)$$

where U_T is a tidal velocity. In the absence of bathymetry and friction then the flow in a re-entrant channel would be exactly U_T. In order to transform our momentum equation to a coordinate system moving with velocity U_T we just subtract (19) from (17). This makes the body force term in (18) vanish, but, because we are in a moving frame of reference, the form drag term appears, and the new volume-integrated energy equation is

$$\begin{aligned} &\frac{\partial}{\partial t}\left[\int_V E' \; dV + \int_{A_o} (1/2)\rho_o g\eta^2 dA \right] \\ &+ \int_{A_{SIDES}} \left[\mathbf{u} - \left(U_T, 0, 0 \right) \right] \cdot \hat{\mathbf{n}} \; E' \, dA \\ &\quad = U_T \int_{A_o} p_B' \frac{\partial \zeta}{\partial x} \; dA \\ &\qquad - \int_{A_{SIDES}} \left[\mathbf{u} - \left(U_T, 0, 0 \right) \right] \cdot \hat{\mathbf{n}} \; p' \, dA \\ &\qquad - \int_V N \, dV \end{aligned} \quad (20)$$

and E' is the same as E, but with $\mathbf{u}$ replaced by $\left[\mathbf{u} - \left(U_T, 0, 0 \right) \right]$. Thus the expression $U_T \int_{A_o} p_B'\zeta_x \, dA$ gives a practical way of calculating the work done by form drag in a time-varying flow, assuming that one can define a suitable U_T.

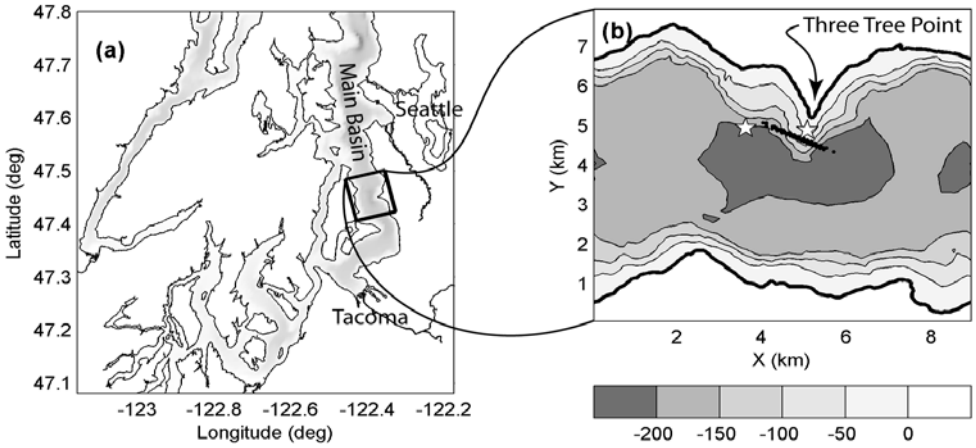

Figure 4. Maps of (a) Puget Sound, Washington, and (b) Three Tree Point (TTP). A local, rotated coordinate system (x, y) is defined in (b) such that flood tide produces positive along-channel flow (to the right). The spatial domain of the numerical model is the region in (b), with bathymetry (m) shown by the grayscale in (b). The line of dots crossing TTP at an angle shows the locations of the microstructure profiler drops.

A Realistic Example, with Observations and a Model

To explore these ideas in a realistic context, we consider stratified, tidal flow past Three Tree Point (TTP) in Puget Sound, WA. In March of 2001, the R/V *Thomas G. Thompson* conducted the first of several cruises at TTP, a sharp headland that juts out ~1 km from the walls of Puget Sound (Fig. 4). Subsurface, TTP is a ridge sloping downwards at a slope of ~1:5 (vertical: horizontal) to a depth in excess of 200 m. The Main Basin of Puget Sound typically has steep sidewalls and a flat bottom at ~200 m due to sedimentary infill of the glacially carved channel. The ~30 m depression off the toe of TTP is common to many points around Puget Sound, and may reflect preferential lack of sediment deposition there due to enhanced tidal currents. The site was selected for the feature's relatively regular shape and isolation from other features. It is a three-dimensional obstacle with sloping walls that permit flow to pass both around and over it. Tidal velocities are on the order of 15 cm s^{-1} when averaged over an across-channel section off TTP (*Lavelle et al*., 1988). In order to study the stirring and mixing that the headland causes, the R/V *Thompson* steamed along the track shown in Fig. 4, completing nine sections in about 1.5 days.

Along the nine across-TTP sections, the turbulent and other properties of the flow were measured by repeat drops of the loosely tethered vertical profiler Chameleon (*Moum et al*., 1995) developed at Oregon State University. Because it can profile all the way to the ocean floor, the data include the bottom boundary layer. Near-surface observations are contaminated by the ship's wake, so the first 10 m of data are discarded. The probe carries an array of instruments to measure temperature and salinity with a vertical resolution of 0.1 m, later averaged to 1 m. The median spacing between Chameleon drops was 107 m, though the spacing varied between sections depending on the ship speed and bottom depth. The sections consist of data taken within a two-hour window centered on the time that the ship crossed the TTP ridge.

We can express the total boundary drag along a section as the sum of three terms: $D = D_{BBL} + D^{\text{int}}_{FORM} + D^{surf}_{FORM}$, where D_{BBL} is the frictional drag from the bottom boundary layer, in the direction of the section, integrated over that section. The other two terms represent the form drag and are divided (based only on observational necessity) into a part associated with pressure perturbations from the deformation of isopycnals (D^{int}_{FORM}) and a part associated with pressure perturbations due to the surface height field (D^{surf}_{FORM}). The Chameleon data were used

to estimate only D_{BBL} and D_{FORM}^{int}. The along-section component of the form drag per unit width W of the bump is calculated as

$$\frac{D_{FORM}^{\text{int}} + D_{FORM}^{surf}}{W} = -\int_{X_1}^{X_2} p_B' \frac{d\zeta}{dx'} dx' \qquad (21)$$

where the product of pressure at the ocean bottom, p_B', and the local, along-section topographic slope, $\zeta_{x'}$, is integrated along the track between the endpoints X_1 and X_2 (Fig. 1) at which the bottom depths are the same. The along-track coordinate is x' and is at an angle to the along-channel direction in the case of the Chameleon sections. Drag is negative when it slows a flow of positive sign, here defined to be flooding/southwards for along-channel flow. In order to calculate p_B^{int} (that portion of p_B' associated with isopycnal displacement), we assume the flow is hydrostatic and integrate

$$p_B^{\text{int}} = \int_{\zeta}^{z_o} g\rho \, dz \qquad (22)$$

from the bottom to a specified near-surface position $z_o = -10$ m. Then (22) is used in (21) to obtain D_{FORM}^{int}. The pressure per unit frontal area is calculated as $D_{FORM}^{\text{int}} / (WH_T)$ where H_T is the height of the obstacle (Fig. 1), which is about 100 m along the section. The barotropic form drag cannot be evaluated from the Chameleon data set, though a calculation will be made from the results of the numerical simulation. The frictional drag was estimated from the Chameleon measurements following *Dewey and Crawford* (1988), using dissipation measurements in the log layer.

Figure 5 shows the evolution of the density field from the Chameleon sections. Each row pairs two sections taken during the same point in the tidal cycle, such as section 3 and section 5 from max flood; sections in the left column were recorded before a storm-related strengthening of near-surface stratification while sections on the right were taken afterwards. Beginning with max flood, the tidal time increases down the rows.

Considering first the less-stratified case, a sharp 50-m dip in the isopycnals occurs downstream (south) of the bump during maximum flood (Fig. 5a); dense fluid heaps up on its upstream side. During early ebb (c), the isopycnals relax to form a moderate depression over the bump. During late ebb, mid-depth isopycnals deepen downstream (north) of the bump (e). During early flood (g), a broad depression forms

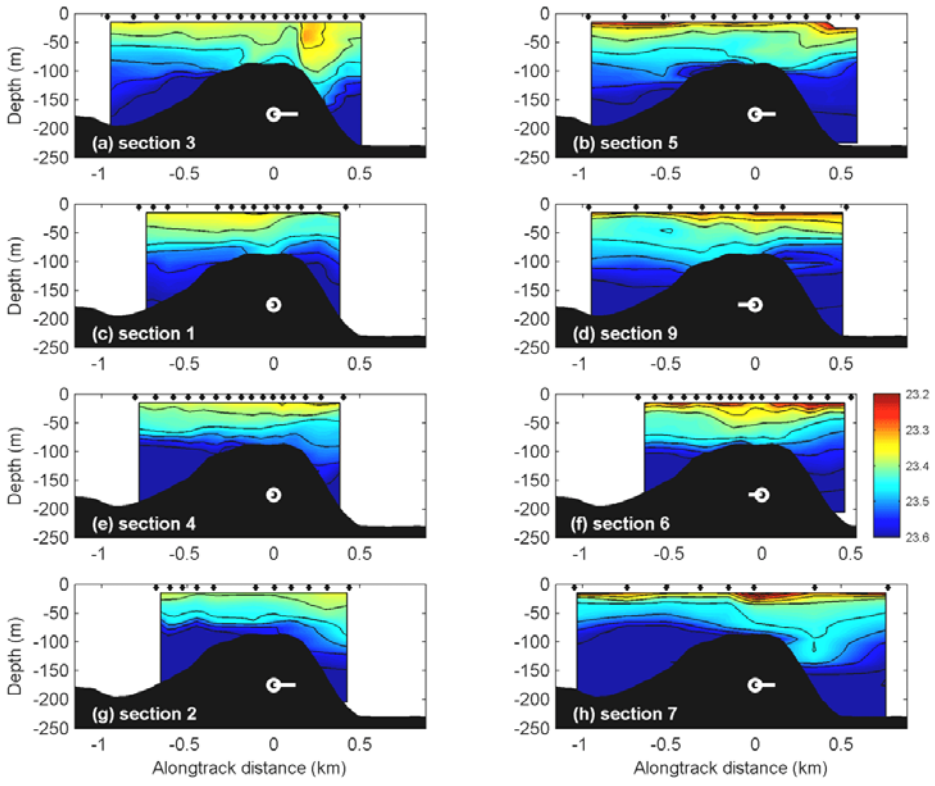

Figure 5. Sections of observed potential density (color scale; contour interval is 0.05 kg m^{-3}) on 8 Chameleon sections (Fig. 4). The perspective is from offshore looking towards the TTP ridge, which is centered at ~0 km in this along-track coordinate system. Drop locations are shown as black diamonds. Sections on the left (right) were taken before (after) an intrusion of low-density surface water. Moving down the rows, the sections progress through a tidal cycle beginning with max flood. The predicted tidal velocity, U_T, is shown in each panel as a white line emanating from a circle; its amplitude can be read from the horizontal axis in units of (m s^{-1}). A spectacular surface-intensified lee wave is apparent in (a).

again on the downstream side of the bump. With the onset of greater surface stratification following the storm (right column), the density field alters. The most significant change is the lack of a sharply defined depression downstream of the bump during max flood (b). During late ebb (f), isopycnals dip across the bump as they did in the less-stratified case, but over a shorter distance. During early flood (h), the asymmetry of isopycnals across TTP is again apparent.

In order to understand the overall importance of TTP, we performed a numerical simulation for a segment of Main Basin centered on TTP, shown in Fig. 4b. The model allows us to calculate the total frictional and form drag on TTP, whereas the microstructure observations only give these on a 2D section. Using the bathymetry of a 9 km by 8 km section of Main Basin, we interpolated the north and south edges of this section to artificially create a re-entrant channel. This avoids the difficulties of open boundaries, and in fact we lack the data to adequately specify properties at the boundaries. The use of a re-entrant channel is reasonable for physical processes which are confined in space during the time period of interest. Near TTP the physical process of greatest importance is the tidal advection of eddies generated at the headland. Because the tidal excursion near TTP is ~3 km, eddies are not likely to be affected by the re-entrant domain for at least a few tidal cycles. We use the Hallberg Isopycnic Model (HIM, *Hallberg and Rhines* 1996), with a Richardson number-dependent turbulence parameterization (*Hallberg,* 2000). The horizontal resolution is 100 m, and there are 20 isopycnal layers, each initially 12 m thick. The density step across layers varies with depth to match the average stratification over the period of Chameleon observations. Since this type of model does not inherently place high vertical resolution near boundaries, it does not in general resolve the details of the bottom boundary layer, unlike a model with a terrain-following coordinate system. Instead, the bottom stress is calculated using a quadratic drag law, with drag coefficient $C_D = 2.5\times10^{-3}$ based on the velocity averaged over the bottom 15 m. This bottom stress is then distributed in the water column by diapycnal fluxes which are governed by the turbulence parameterization. This gives rise to boundary layers of realistic thickness where the vertical resolution is great enough, although here the boundary layers are not well-resolved.

The sole dynamical forcing is an along- and across-channel body force, designed to simulate the *Lavelle et al.* (1988) predicted along-channel tidal velocity at this location and time, U_T. We constructed an analytical version of U_T by fitting it with 6 tidal constituents (M2, S2, N2, K1, O1, and P1) for a 28 day time period around the cruise. The analytical form had less than 6% rms difference from the original signal. The body force then was calculated from the equations:

$$\frac{\partial U_T}{\partial t} - fV_T = \varphi^x, \quad \frac{\partial V_T}{\partial t} + fU_T = \varphi^y \qquad (23)$$

Here U_T and V_T are the predicted, cross-channel averaged, tidal velocities we wish to force, and by definition $V_T = 0$ since there is no net across-channel transport. We force the model with the horizontal, time-dependent acceleration $\left(\varphi^x, \varphi^y\right)$ due to a fictitious body force, obtained as an integral of (23). This force is analogous to that due to a gradient of the surface height field held constant over the numerical domain, which is a reasonable approximation for this region of Main Basin. In the absence of irregular topography and friction, this form of forcing would exactly reproduce the desired along-channel velocity, U_T. With realistic bathymetry and boundary stress, there is net drag acting on (23) which would cause the resulting volume-average of U_T to have smaller amplitude than desired, and some phase lead. We proceed assuming that these are small, and rely on comparisons with current meter observations to assess whether the forcing is reasonably correct.

The model simulation was started from rest at a time when the predicted tidal velocity was zero, and was run for 216 lunar hours (a lunar hour is defined as 12.42/12 hours). The model was run for 83 lunar hours before the first Chameleon section. Typical output fields are plotted in Fig. 6. It can be seen that TTP causes both a strong tidal headland eddy and significant deformation of isopycnals reminiscent of a lee wave. The headland eddies survive long enough to interact with the opposite-signed eddy of the following tide, and may form dipoles. The relative longevity of these eddies may be due to the depth of the

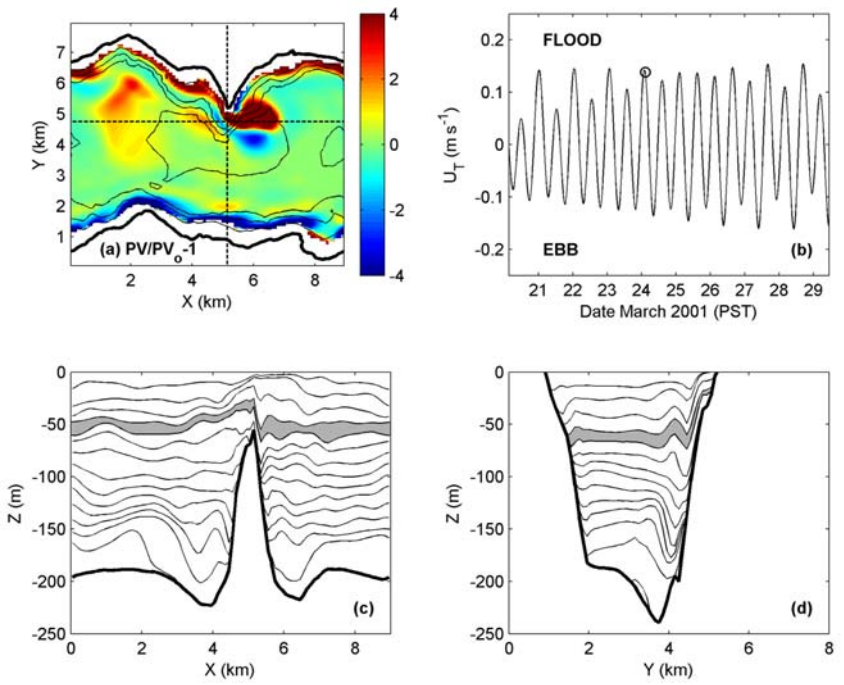

Figure 6. Typical model output fields at a time close to max flood (flow to right). The normalized potential vorticity of the 5th layer from the top is mapped in (a). The predicted tidal velocity for the entire run is shown in (b), with the snapshot time shown as a circle. The distortion of isopycnal layer interfaces is plotted for along-channel (c) and across-channel (d) sections, on the dashed lines in (a). The layer from (a) is shown in gray. A strong cyclonic or "flood" (red) eddy has just being released from TTP with an older "ebb" (blue) eddy offshore of it. The eddy is accompanied by large isopycnal displacements. The contour interval between density interfaces is not constant because all layers are initially 12 m thick, but the stratification is greater near the surface.

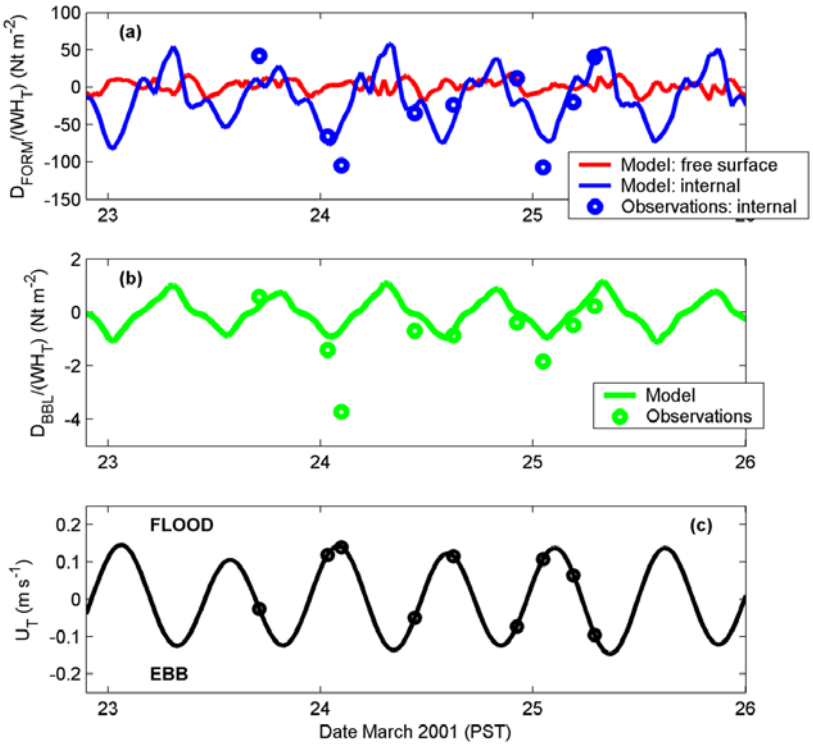

Figure 7. Form drag (a) per unit frontal area, on the Chameleon section, comparing the model results (lines) with values from the 9 Chameleon sections (circles). The frictional drag per unit frontal area is plotted in (b), and the timing of the sections relative to U_T is shown in (c).

water, which makes the effect of bottom friction small. The interaction of such eddies has been found by *Pawlak and MacCready* (2002) to be an effective way of driving mean flow either toward or away from TTP.

The model drag terms, integrated along the Chameleon section, are plotted against time in Fig. 7. On this section D_{FORM}^{int} dominates over D_{FORM}^{surf} (Fig. 7a), and D_{BBL} is smaller than both by a factor of 10-50. The same integrated drag terms from the 9 Chameleon sections are plotted as circles on Fig. 7. There is reasonable agreement between the model and observations, except that the drag is significantly underpredicted on ~three occasions. One of these is Chameleon section 3, where the model does not reproduce the large downwelling of light surface water in the lee of the ridge which would contribute to the form drag. The model also underpredicts the frictional drag for section 3.

The results from Fig. 7 give reasonable confidence in the model form and frictional drags, so we turn next to the full volume-integrated drag budget, Fig. 8. Here the frictional drag is again negligible, having just 6% of the standard deviation of the form drag. The two form drag terms are now roughly equal in magnitude. We have found from numerical experiments (not shown) that the ratio $D_{FORM}^{\text{int}} / D_{FORM}^{surf}$ increases with distance from TTP. This is physically reasonable because the eddy (associated loosely with D_{FORM}^{surf}) is strongest in sections taken at the tip of TTP and in its lee. On the other hand the baroclinic response is greater in deeper water.

In Fig. 8b we plot the volume-integrated rate of work performed by the sum of the model drag terms. This is calculated as $U_T \times D$ (following Eqn. 20), and we find that the time-averaged rate of conversion of barotropic tidal energy into waves, eddies, and eventually dissipation, is 0.72 MW. How can we tell if this is a reasonable number? The only available comparison comes from the section-averaged tidal model of *Lavelle et al.* (1988). They used a linear drag on their section-averaged currents in order to match observed M_2 heights and phases throughout Puget Sound. The dynamics on a given cross-section were governed by the equation:

$$\frac{\partial U_T}{\partial t} = -g\frac{\partial \eta}{\partial x} - \frac{r}{\langle H \rangle} U_T \qquad (24)$$

where $\langle H \rangle$ is the average depth on that section. They varied r as the tuning parameter, and in all the deep channels, including Main Basin where TTP is located, used $r = 2 \times 10^{-3}$ m s^{-1}. This is roughly equivalent to having a quadratic drag coefficient of $1 - 2 \times 10^{-2}$, or 4 to 8 times greater than typical values. We plot the rate of work that would be done by this drag term in Fig. 8b. It is somewhat smaller in magnitude than our model results, does not have the phase lead relative to U_T, and does not change sign. Remarkably, however, its mean value, 0.86 MW, is quite close to the model mean.

One interpretation of the above result (admittedly generous to our model) is that our model and observations provide a physical explanation for the high friction *Lavelle et al*. (1988) found necessary to model the tides. The evidence strongly suggests that their estimated friction was essentially correct, but that the "friction" was not really friction at all. Rather, it was caused mostly by form drag on large features of rough topography such as TTP. It remains for future research to determine if these form drag results hold for other regions of Puget Sound, but topographic features like TTP are abundant in the region.

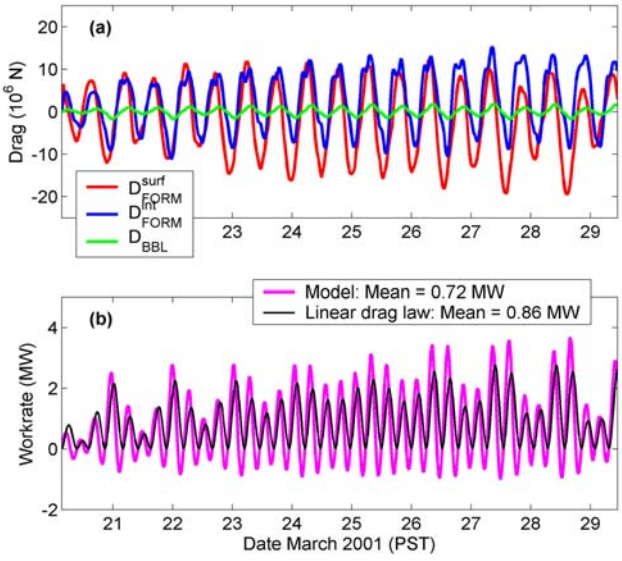

Figure 8. Volume-integrated drag terms versus time (a) from the numerical model. The form drag terms are much larger than the frictional drag. The rate of work performed by the sum of the model drag terms is plotted in (b), and is compared with the workrate calculated from the linear tidal model of *Lavelle et al.* (1988).

Summary and Conclusions

The form drag mechanisms seen here have important implications for the mixing of tracers in coastal and near-boundary regions. Standard boundary layer drag enhances mixing only near the topography. This may be an inefficient generation mechanism for buoyancy flux, because stratification in the boundary layers is generally lower than in the interior. Form drag, on the other hand, tends to project its flow disturbances over the full depth of the water column, and over a volume similar to the product of the projected frontal area of the obstacle and the tidal excursion. Thus form drag can cause turbulent mixing throughout the water column. Further, horizontal eddy structures shed by the obstacle (Fig. 6) are an excellent means for stirring fluid away from the mixing region which is constantly replaced by new, unmixed fluid.

Acknowledgments. We are indebted to Jim Moum, Jodie Klymak, and Sasha Perlin (OSU) for their Chameleon data at TTP. Robert Hallberg (GFDL) provided almost daily assistance with the numerical modeling, along with David Darr (UW). We had many helpful conversations with Eric D'Asaro and Eric Kunze (UW), and Jonathan Nash (OSU). This work was supported by the ONR Scholar of Oceanography Award and NSF grant OCE-0099058.

References

Baines, P. G., Topographic effects in stratified flows. Cambridge University Press, Cambridge, 482 pp., 1995.

Davies, H. C., and P. D. Phillips, Mountain Drag along the Gotthard Section during ALPEX. *J. Atmos. Sci.*, **42**, 2093-2109, 1985.

Dewey, R. K., and W. R. Crawford, Bottom stress estimates from vertical dissipation rate profiles on the continental shelf. *J. Phys. Oceanogr.*, **18**, 1167- 1177, 1988.

Foreman, M. G. G., R. A. Walters, R. F. Henry, C. P. Keller, and A. G. Dolling, A tidal model for eastern Juan-de-Fuca Strait and the southern Strait of Georgia. *J. Geophys. Res.*, **100**, 721-740, 1995.

Gill, A. E., Atmosphere-Ocean Dynamics. Academic Press, San Diego, 662 pp., 1982.

Hafner, T. A., and R. B. Smith, Pressure Drag on the European Alps in Relation to Synoptic Events. *J. Atmos. Sci.*, **42**, 562-575, 1985.

Hallberg, R., Time integration of diapycnal diffusion and Richardson number-dependent mixing in isopycnal coordinate ocean models. *Mon. Weather Rev.*, **128**, 1402-1419, 2000.

Hallberg, R., and P. B. Rhines, Buoyancy-driven circulation in an ocean basin with isopycnals intersecting the sloping boundary. *J. Phys. Oceanogr.*, **26**, 913-940, 1996.

Jayne, S. R., and L. C. St. Laurent, Parameterizing tidal dissipation over rough topography. *Geophys. Res. Lett.*, **28**, 811-814, 2001.

Killworth, P. D., and M. M. Nanneh, Isopycnal momentum budget of the Antarctic Circumpolar Current in the Fine Resolution Antarctic Model. *J. Phys. Oceanogr.*, **24**, 1201-1223, 1994.

Kundu, P. K., and I. M. Cohen, *Fluid Mechanics*, Second Edition. Academic Press, San Diego, 730 pp., 2002.

Lavelle, J.W., H.O. Mofjeld, E. Lempriere-Doggett, G.A. Cannon, D.J. Pashinski, E.D. Cokelet, L. Lytle, and S. Gill, A multiply-connected channel model of tides and tidal currents in Puget Sound, Washington and a comparison with updated observations. NOAA Tech. Memo. ERL PMEL-84 (PB89-162515), 103 pp., 1988.

Ledwell, J. R., E. T. Montgomery, K. L. Polzin, L. C. St. Laurent, R. W. Schmitt, and J. M. Toole, Evidence of enhanced mixing over rough topography in the abyssal ocean. *Nature*, **403**, 179-182, 2000.

Lott, F., and M. J. Miller, A new subgrid-scale orographic drag parameterization: Its formulation and testing. *Q. J. Roy. Met. Soc.*, **123**, 101-127, 1997.

MacCready, P. M., and G. Pawlak, Stratified flow along a corrugated slope: Separation drag and wave drag. *J. Phys. Oceanogr.*, **31**, 2824-2839, 2001.

MacCready, P., and P. B. Rhines, Meridional Transport Across a Zonal Channel: Topographic Localization. *J. Phys. Oceanogr.*, **31**, 1427-1439, 2001.

Moum, J. N., M. C. Gregg, R. C. Lien, and M. E. Carr, Comparison of turbulence kinetic energy dissipation rate estimates from two ocean microstructure profilers. *J. Atmos. Tech.*, **12** (2), 346-366, 1995.

Moum, J. N., and J. D. Nash, Topographically induced drag and mixing at a small bank on the continental shelf. *J. Phys. Oceanogr.*, **30**, 2049-2054, 2000.

Marshall, J., D. O. Olbers, H. Ross, and D. Wolf-Gladrow, Potential vorticity constraints on the dynamics and hydrography of the Southern Ocean. *J. Phys. Oceanogr.,* **23,** 465-487, 1993.

Moum, J. N. and J. D. Nash, Topographically induced drag and mixing at a small bank on the continental shelf. *J. Phys. Oceanogr.*, **30**, 2049-2054, 2000.

Munk, W. H., and E. Palmén, Note on the dynamics of the Antarctic Circumpolar Current. *Tellus*, **3**, 53-55, 1951.

Nash, J. D. and J. N. Moum, Internal hydraulic flows on the continental shelf: High drag states over a small bank. *J. Geophys. Res.*, **106**, 4593-4611, 2001.

Pawlak, G. and P. MacCready, Oscillatory flow across an irregular boundary. *J. Geophys. Res.,* **107,** 4-1-to 4-17, 10.1029/2000JC000596, 2002.

Schär, C., Mesoscale mountains and the larger-scale atmospheric dynamics: A review. *Meteorology at the Millennium*, Academic Press, 29-42, 2002.

Smith, R. B., A Measurement of Mountain Drag. *J. Atmos. Sci.*, **35**, 1644-1654, 1978.

Thorpe, S. A., The generation of internal waves by flow over the rough topography of a continental slope. *Proc. R. Soc. Lond. A*, **439**, 115-130, 1992.

Thorpe, S. A., The cross-slope transport of momentum by internal waves generated by alongshore currents over topography. *J. Phys. Oceanogr.*, **26**, 191-204, 1996.